



HAL
open science

Influence of manufacturing orientations on the morphology of alloy 718 single struts manufactured by selective laser melting

Mathieu Suard, Ludovic Barrière, Pierre Lhuissier, Simon Perusin, Benoit Filloux, Rémy Dendievel

► To cite this version:

Mathieu Suard, Ludovic Barrière, Pierre Lhuissier, Simon Perusin, Benoit Filloux, et al.. Influence of manufacturing orientations on the morphology of alloy 718 single struts manufactured by selective laser melting. *Material Design & Processing Communications*, 2020, 3, 10.1002/mdp2.140 . hal-03427104

HAL Id: hal-03427104


<https://hal.science/hal-03427104v1>

Submitted on 12 Nov 2021

HAL is a multi-disciplinary open access archive for the deposit and dissemination of scientific research documents, whether they are published or not. The documents may come from teaching and research institutions in France or abroad, or from public or private research centers.

L'archive ouverte pluridisciplinaire **HAL**, est destinée au dépôt et à la diffusion de documents scientifiques de niveau recherche, publiés ou non, émanant des établissements d'enseignement et de recherche français ou étrangers, des laboratoires publics ou privés.

Influence of manufacturing orientations on the morphology of alloy 718 single struts manufactured by selective laser melting

Mathieu Suard^{1,2}  | Ludovic Barrière¹ | Pierre Lhuissier² | Simon Perusin¹ | Benoit Filloux³ | Rémy Dendievel²

¹Institute of Technology (IRT) Saint Exupéry, Toulouse Cedex 4, France

²CNRS, Grenoble INP, SIMAP, Univ. Grenoble Alpes, Grenoble, France

³Altran Technologies, Blagnac, France

Correspondence

Mathieu Suard and Ludovic Barrière, Institute of Technology (IRT) Saint Exupéry, 3, rue Tarfaya - CS 34436, 31405 Toulouse Cedex 4, France.

Email: mathieu.suard@irt-saintexupery.com; ludovic.barriere@irt-saintexupery.com

Abstract

Selective laser melting (SLM) is of great interest for manufacturing lightweight structures such as lattices. It allows a broad range of lattice topologies to be created. However, when manufacturing small struts, roughness, lack of dimensional accuracy, and porosity level can decrease their mechanical properties and thus affect the mechanical response of the entire structure. This study focuses on the high-resolution characterization of alloy 718 (UNS N07718) single struts (constitutive elements of the lattice) manufactured by SLM. Process parameters, strategy, and post-treatments remain constant while varying strut positions on the build plate and orientations. A methodology for the systematic characterization of 19 struts with high-resolution X-ray tomography has been developed. Different features related to the strut size, shape, waviness, roughness, and porosity are extracted. The analysis of those features when varying strut positions and orientations highlights the influence of each parameter. The build orientation is a first-order parameter influencing strut morphology as already referenced in the literature. This systematic study reveals also the influence of the in-plane orientation for inclined struts that alters their roughness, shape, and size.

KEYWORDS

Build orientation, In-plane orientation, Lattice structures, Selective Laser Melting, Single struts, X-ray tomography

1 | INTRODUCTION

Lattice structures are made out of a network of interconnected struts. They exhibit unique characteristics that monolithic materials cannot offer. Such characteristics are, for example, high stiffness-to-weight ratio,¹⁻⁵ improved energy absorption,⁶ optimized heat transfer,^{7,8} and optimization of surface topology for osseointegration.^{9,10} Within this family, periodic lattice structures are composed of a repetition of a unit cell. Their topology and relative density can be tuned to achieve required properties.

The recent development of additive manufacturing (AM) techniques allows a larger freedom in designing parts. Various studies have been focused on manufacturing lattice structures with powder-based AM techniques.¹¹⁻¹⁴ This study will focus on the characterization of lattice structures made by SLM.

Powder-bed AM techniques come along with limitations linked to their process parameters and scan strategies. When manufacturing small struts, defects can appear. Knowing the origin and amplitude of such defects is of major importance in order to control the mechanical properties of lattice structures. Studies focusing on the characterization of lattice structures have already determined some links between process parameters, inherited defects, and the related mechanical behavior as compared with the expected one.¹⁵⁻²⁴ Defects are usually characterized using X-ray tomography at the scale of the struts. They can be sorted into different categories:

1.1 | Geometrical defects

- Size: For cylindrical struts, diameters are calculated with different approaches. Inscribed and circumscribed diameters are frequently determined.^{19,22}
- Shape: The difference between the ideal shape (usually a cylinder with circular cross section) and the manufactured one. The manufactured cross section could be elliptical due to overmelting on the down-facing surfaces.^{19,21} It can be quantified by using an equivalent ellipse to determine its shape ratio.
- Waviness: The waviness of the neutral fiber of the strut as compared with the neutral axis of the CAD model.

1.2 | Surface defects

- Roughness: Line roughness can be calculated isolating line profiles along strut axis. Studies reported calculation of arithmetic roughness and maximum height of profile.^{19,20,22}
- Surface defect: Isolating surface defects and analyzing their morphology, sharpness, and depth allowed also the understanding of mechanical response of struts especially in fatigue.²⁵

1.3 | Internal defects

- Porosity: Porosity ratio, pores size distribution, and pores morphology have been studied in several studies.¹⁸⁻²⁰ Many types of porosity can be found such as internal pores in the raw material, lack-of-fusion, or hey-hole effect.²⁶

The quantification of the strut size is the most evaluated parameter. Liu et al.¹⁶ showed that for SLM-manufactured struts in AlSi10Mg alloy, the strut diameter—determined at each slice by fitting a circle to the surface—is larger than the nominal one for inclined and horizontal struts but is lower for vertical struts. Dallago et al.¹⁵ highlighted the same trend for Ti-6Al-4V struts manufactured by SLM.

In most of the studies, defects are analyzed and quantified to be implemented in simulations at the scale of the lattice. Strut orientation effect on porosity level in AlSi10Mg alloy has been investigated by Delroisse et al.¹⁸ They highlighted a higher level of porosity on inclined struts due to a larger time spent at high temperature for the “down-facing” zone. However, there is a lack for a complete study of the morphology of the struts as a function of their position and orientations.

A previous study focused on the development and validation of a mechanical equivalent diameter for EBM lattice structures.¹⁹ This work utilize similar methodology to link strut positions and orientations with defects type, magnitude, and morphology. Their position in the build envelope, build orientation, and in-plane orientation are the investigated parameters. High-resolution X-ray tomography is systematically used to quantify strut defects.

2 | MATERIALS AND METHODS

2.1 | Manufacturing and materials

2.1.1 | Raw material

The raw material used in this study is alloy 718 (UNS N07718) gas atomized powder provided by Aubert & Duval. Its chemical composition is listed in Table 1. The particles are spherical with a unimodal particle size distribution. They exhibit a 29.5 μm median diameter with 80% of the diameters between 15 and 54 μm .

TABLE 1 Chemical composition in weight of the principal elements of the native powder

Element	Ni	Cr	Fe	Nb	Mo	Ti	Al	Co	C	Si	O
wt%	53.9	19.1	17.2	5.36	3.15	1.03	0.44	<0.1	0.036	0.028	0.012

2.1.2 | Manufacturing and post-treatment

Parts are manufactured using an EOS M290 machine with a layer thickness of 40 μm and a build envelope of 250 mm \times 250 mm \times 325 mm. A stainless steel recoater is used. The process parameters used in this study have been set to reduce the well-known overmelting phenomenon on overhanging surfaces.^{18,19,27} For that purpose, scan speed and scan power have been increased compared with the supplier recommended parameters. The melting strategy used is based on hatching without contouring. As explained in literature,^{28,29} the repeated melting and solidification steps during SLM process induces a heterogeneous solidification rate, thus thermal contraction within the parts. This thermally induced strain could lead to a nonrespect of the CAD dimensions and build errors when the recoater hit the parts. To limit that effect, the use of contours has been proscribed.

After production, parts undergo classical homogenization and two-steps aging under primary vacuum (10^{-5} bar). No post-treatments for optimizing roughness and porosity were used.

2.1.3 | Structures of interest

This study aims at analyzing morphology of BCCZ lattice structures produced by Selective Laser Melting (SLM). A unit-cell of such a structure is represented in Figure 1A. It is composed of vertical and inclined struts oriented at 35.3° from the build plane. The strut's diameter D_{CAD} is set to 1 mm, and the length of the vertical strut is set to $L_V = 7$ mm. Inclined struts have a length $L_I = 6.06$ mm.

The morphology of the constitutive elements of the lattice structure is analyzed in this study. Vertical and inclined struts have thus been designed with a diameter D_{CAD} and a length L_V and L_I , respectively (see Figure 1B).

Struts are placed between two parallelepipeds to place the grips for a further uniaxial tensile testing. In order to ensure manufacturability of those samples and to ensure a thermal environment similar to the one of the lattice, lattice supports have been designed and are removed by electrical discharge machining before X-ray tomography. The gauge length of the sample is not supported to respect the same thermal conditions as inside the lattice structure.

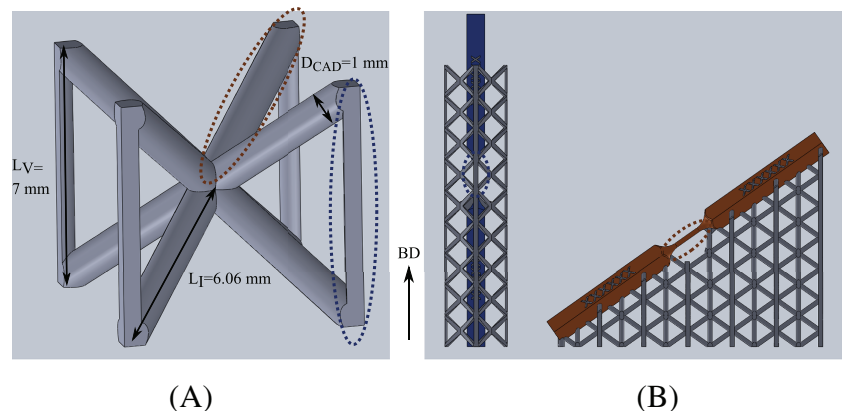


FIGURE 1 A, Unit-cell of interest with its characteristics. B, Microstruts samples composed of constitutive elements of the lattice: vertical (blue) and inclined strut (orange)

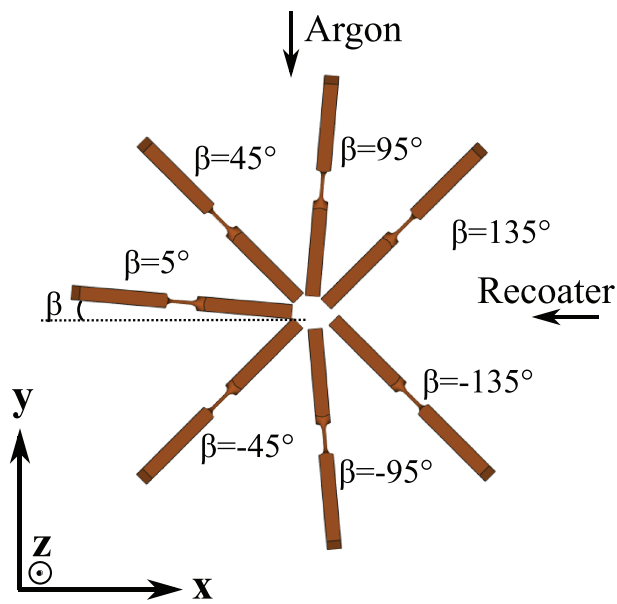


FIGURE 2 Design space corresponding to the different in-plane orientations for inclined struts (top view)

2.1.4 | Parameters of interest

Keeping process parameters and strut diameter constant, a focus has been made on evaluating the effect of strut positions and orientations.

Microstruts are placed at different positions within the build plate using a Latin hypercube sampling method. Origins of x-axis and y-axis are on the lower left corner of the build plate (see Figure 2). Vertical and inclined samples are printed. Their orientation from the build plane is $\alpha = 90^\circ$ and $\alpha = 35.3^\circ$, respectively. It is commonly denominated as the *build orientation*. The recoater and argon flow directions are represented by arrows in Figure 2.

For inclined samples, the orientation around the build direction (z-axis) is also a parameter of interest ($\beta = [-135^\circ:135^\circ]$). It will be denoted as *in-plane orientation*. As explained earlier, due to differences in solidification and thermal contractions, the zone on the down-facing side can rise as shown in red in Figure 3. The recoater could then hit the part during manufacturing. To avoid critical build error, orientations facing the recoater movement are avoided ($\beta > 135^\circ$ and $\beta < -135^\circ$). The $\beta = 0^\circ$ orientation is also avoided for similar reasons.

Nineteen samples were analyzed by X-ray tomography in order to assess their morphology and quantify their defects (six verticals and 13 inclined).

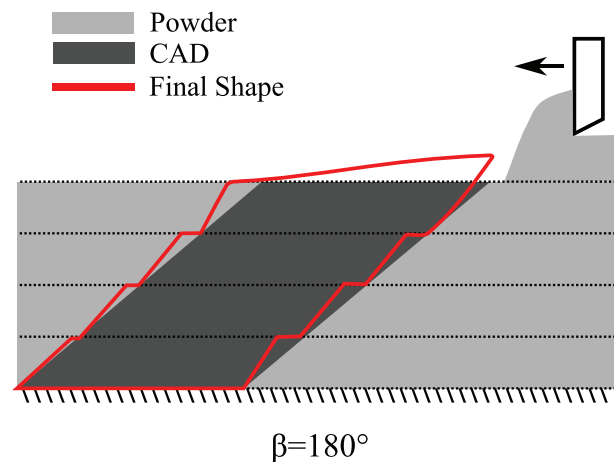


FIGURE 3 Schematic showing the recoater spreading powder onto an inclined strut with an in-plane orientation of 180° . The red part represents deviation of shape due to thermal distortion during manufacturing

2.2 | X-ray tomography analysis

2.2.1 | Experimental procedure

The morphology of the struts is assessed using an X-ray tomograph (RX Solutions Easytom XL) equipped with a nanofocus LaB₆ source and a flat panel detector. A 1- μm thick W cathode is used. The source tension and intensity are kept constant at 100 kV and 25 μA , respectively. The beam is filtered with a copper plate of 0.5 mm. To be able to visualize small pores, a magnification of 63.5 is set leading to a voxel size of 2 μm . The visualization of the entire gauge length thus requires a helical scan with 2784 projections, and five turns over a translation of 14 mm. The duration of a scan is roughly 45 minutes.

Reconstruction is performed with the dedicated RX Solution software using filtered-back projection algorithm. For each scan, the same beam hardening filter is used. Volumes are rotated along their neutral axis to align the down-facing surface at the same angle for each inclined sample.

2.2.2 | Extracted features

A 3D median filter of radius 1 pixel is applied prior to thresholding. Two threshold values are set for a better estimation of internal and external porosity to counteract a slight beam hardening effect. From the binary image, quantitative data are systematically extracted. An ImageJ³⁰ script has been developed to extract morphological features of the struts. The first step of the script corresponds to a fine alignment of the neutral axis of the strut with the z direction of the 3D volume. To do so, the image is rotated around its x-axis and y-axis. For each configuration, the common surface area of the strut in the z direction is calculated. The strut is considered aligned for x and y angles maximizing this common surface.

Strut size

The definition of a strut diameter is not straightforward as its shape is not a perfect cylinder. Therefore, four different diameters are extracted:

- D_{insc} is the *inscribed diameter* calculated from the inscribed surface. It is defined as the common area of all the slices of the volume in its neutral axis direction.
- D_{circ} is the *circumscribed diameter* calculated from the projection of the surface of every slice of the volume, ie, the circumscribed surface.
- D_{EQ}^V is the diameter of a perfectly circular cylinder having the same volume and height as the strut. It is called the *iso-volume equivalent diameter*.
- D_{EQ} is the *mechanical equivalent diameter* calculated from a fast Fourier transform (FFT) simulation directly from the volume as explained by Suard et al.¹⁹ It corresponds to the diameter of a perfectly circular cylinder having the same stiffness as the scanned one.

D_{insc} , D_{circ} are calculated using the inscribed or circumscribed surface (S) as $D = \sqrt{\frac{4S}{\pi}}$. D_{EQ}^V is calculated using the volume V_s and height h_s of the strut as $D_{\text{EQ}}^V = 2\sqrt{\frac{V_s}{\pi h_s}}$.

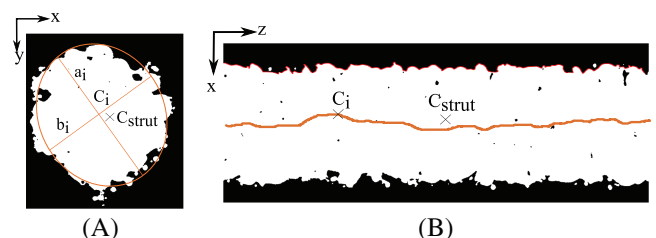


FIGURE 4 A, Transverse cross section at slice i , equivalent ellipse with major axis (a_i), minor axis (b_i). B, Longitudinal cross section of a strut with its variation of neutral fiber position (orange). The center of mass at slice i is placed (C_i). The upper profile (red) is analyzed for roughness calculation

Strut shape

For analyzing the strut shape, the shape deviation from a perfect cylinder is computed. Figure 4A exhibits a slice of a strut and its equivalent ellipse. It is calculated as the ellipse having the same matrix of inertia as the slice. From its major and minor axis, the shape deviation is calculated as the mean value of the difference between the ideal shape ratio (1) and each ellipse shape ratio (b_i/a_i) for all slices i , such as

$$Shape = \left\langle \left| 1 - \frac{b_i}{a_i} \right| \right\rangle_z \quad (1)$$

Waviness

The waviness of the strut is assessed by comparing the Euclidian distance in the x-y plane of the center of mass of the slice (C_i) and the one of the whole strut (C_{strut}) as shown in Figure 4B. The mean neutral fiber deviation is calculated as

$$W = \left\langle \sqrt{(x_{C_{strut}} - x_{C_i})^2 + (y_{C_{strut}} - y_{C_i})^2} \right\rangle_z \quad (2)$$

Roughness

To evaluate the surface roughness, the profile of the strut (as seen in Figure 4) is extracted every 10° around the strut axis. For each profile j , an arithmetic roughness (R_a^j) and a maximum height of profile (R_t^j) are calculated:

$$R_a^j = \frac{1}{L} \int_0^L |r(l)| dl \approx \frac{1}{L} \sum_0^L |r(l)|, R_t^j = r_{\max} - r_{\min}. \quad (3)$$

For each strut, the mean arithmetic roughness $Ra = \langle R_a^j \rangle$ and the maximum height of profile $Rt = \max(R_t^j)$ are extracted.

Porosity analysis

Each pore is isolated and labeled, and several features are extracted such as its volume, center of mass, and external surface. From those features, the pore size distribution, median pore diameter, pore spatial distribution, and pore morphology can be calculated.

For a systematic analysis and comparison, three variables are considered:

- Porosity: $P = \frac{\sum V_{\text{pores}}}{\sum V_{\text{pores}} + V_{\text{strut}}}$.
- Median pore diameter D_{50} . Pore diameters are calculated using the diameter of a sphere having the same volume as the pore.
- Sphericity index: $Sph = 6V \sqrt{\frac{\pi}{S}}$. It ranges between 0 and 1 and is equals to 1 for a sphere.

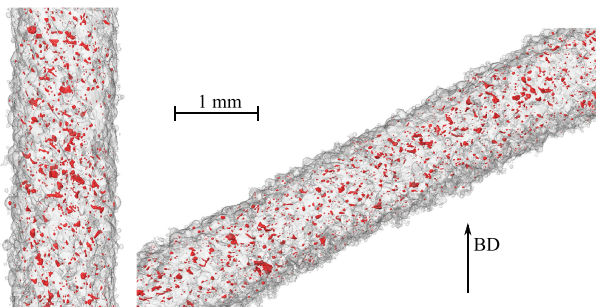


FIGURE 5 Three-dimensional visualization of a vertical strut and an inclined one. BD represents the build direction. Red volumes represent internal porosities

3 | EFFECT OF STRUT INCLINATION FROM THE BUILD PLANE (BUILD ORIENTATION)

The use of X-ray tomography enables the qualitative and quantitative analysis of strut defects. Figure 5 shows a zoom of the 3D representation of a vertical strut and an inclined one. The strut size seems to be close to the nominal diameter (1 mm). The surfaces present two types of defects. Some particles are stuck on the surface without prior melting especially on the down-facing surface. The other surface irregularity, which induces a larger surface roughness, seems to be linked to a poor control of the melt pool from one layer to another. It can be attributed to the absence of contour in the scanning strategy. Pores are represented in red. Qualitatively, they seem to be spread quite homogeneously throughout the strut and exhibiting an irregular morphology.

3.1 | Size

As explained in Section 2.2.2, different diameters are computed from the 3D image of the strut. They are listed in Table 2. Globally, vertical struts exhibit slightly smaller diameters than inclined ones. This is due to the well-known “overmelting” on the down-facing surfaces.^{19,21} The use of the four different diameters give broad information about the consequence of overmelting on the dimension of struts. The largest difference between vertical and inclined struts is for the isovolume equivalent diameter (+7%). In the meantime, the mechanical equivalent diameter (D_{EQ}) does not fluctuate largely. As explained by Suard et al.,¹⁹ the mechanical equivalent diameter allows the discrimination of the volume that does not contribute to carry the load. Overmelting occurring in inclined struts seems thus to induce an increase of the global volume without a significant increase of the mechanically efficient volume.

3.2 | Waviness and shape

The waviness of the strut is the mean deviation of the strut's axis across its length. It is of 12 μm and 19 μm for vertical and inclined struts, respectively. This difference is also due to the overmelting phenomenon leading to difficulties to control the melted area. As a comparison, Lozanovski et al.²¹ computed the waviness of Inconel 625 inclined struts with a 300 μm diameter. Their mean waviness is around 50 μm . The difference of waviness compared with this study can be explained by the difficulty to control precisely the melt pool location for melting struts with such a small diameter.

The mean shape deviation is of 0.05 for vertical struts and 0.10 for inclined ones. Inclined struts are elongated in the build direction due to the overmelting phenomenon.

TABLE 2 Mean values of size features for vertical and inclined struts

$\alpha, ^\circ$	$\langle D_{EQ}^V \rangle, \text{mm}$	$\langle D_{\text{invc}} \rangle, \text{mm}$	$\langle D_{\text{circ}} \rangle, \text{mm}$	$\langle D_{EQ} \rangle, \text{mm}$
Vertical	0.98	0.69	1.15	0.92
Inclined	1.05	0.71	1.21	0.93
Difference	7%	3%	5%	1%

TABLE 3 Mean values of porosity features for vertical and inclined struts

$\alpha, ^\circ$	$\langle P \rangle, \%$	$\langle D_{50} \rangle, \mu\text{m}$	$\langle Sph \rangle$
Vertical	0.33	7.0	0.78
Inclined	0.22	8.1	0.79
Difference	-32%	13.5%	<1%

TABLE 4 Influence of in-plane orientations on their morphological features for inclined struts

β	Size			Waviness and Shape		Roughness		Porosity			
	D_{EQ}^V	D_{invc}	D_{circ}	D_{EQ}	W	Shape	R_a	R_t	D_{50}	P	Sph
			2.6E-03	4.9E-02		1.5E-02	1.6E-02	1.5E-02			

Note. Green values represents P values lower than .05 and red ones indicates P values greater than .05.

3.3 | Roughness

The mean arithmetic roughness R_a and maximum height of profile R_t both increase for inclined struts compared with vertical ones. R_a increases from 18 to 24 μm and R_t from 195 to 241 μm . It is in accordance with an increase of the global volume while keeping a constant mechanical equivalent diameter (explained in Section 3.1). The overmelting phenomenon seems thus to increase the roughness of the struts by increasing the depth of melt pool in the build direction without increasing its mechanical equivalent diameter.

3.4 | Porosity

Mean values of porosity, median diameter, and sphericity index are reported in Table 3.

The median pores diameter and sphericity are rather constant between vertical and inclined struts. Median pore diameter is around 7 μm , but pores as large as 60 μm are present within the struts. Elongated pores are frequently visible in the struts (sphericity index = 0.78). They are spread across the width and length of the struts regularly (see Figure 5). This type of porosity is supposed to be linked to the high speed and high power scan strategy leading to a bad overlapping between two melt pools.

The mean porosity decreases from 0.33% to 0.22% when comparing vertical struts and inclined ones. Since the pores are due to a bad overlapping of the melt tracks, when melting inclined struts, the heat accumulates on the down-facing surface inducing larger melt pools and thus reducing porosity.

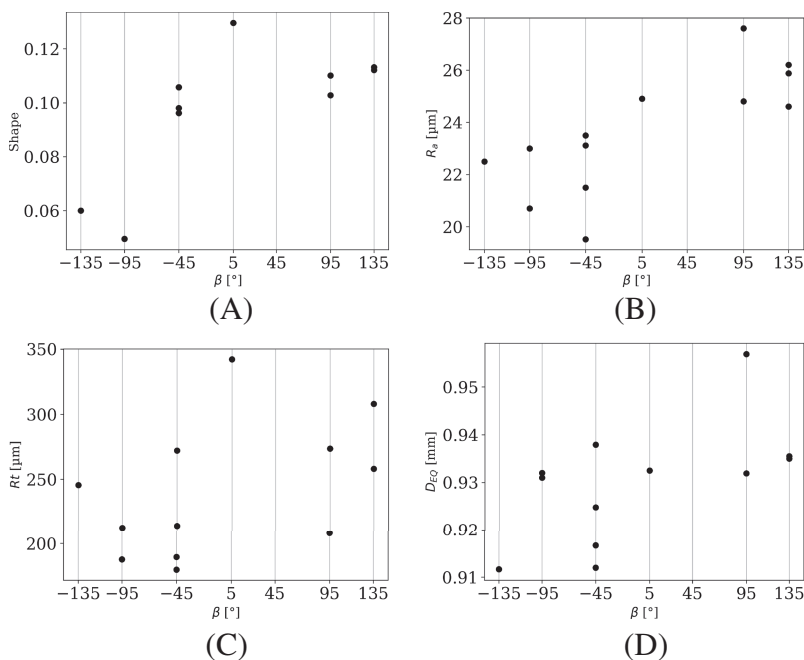


FIGURE 6 Variation of shape deviation, roughness (R_a , R_t) and mechanical equivalent diameter as a function of the in-plane orientation for inclined struts

4 | SECOND-ORDER PARAMETER

4.1 | Sensitivity analysis

For the nineteen samples analyzed, morphological features are extracted. Each sample corresponds to a specific position, build orientation, and in-plane orientation. In order to understand the effect of other parameters on the morphological features of the struts, a one-way analysis of variance (ANOVA) sensitivity analysis has been carried out using *statsmodel* package from python. For each feature, the influence of each parameter is computed independently from the other ones. This methodology gives trends to understand second-order parameter influence. The output of the calculation is a P value resulting from the Fisher acceptance test. It is set that the parameter is influential if the resulting P value is lower than .05.

The sensitivity analysis has been carried out on vertical struts and inclined struts separately. It has shown that the *position of the struts within the build plate has no effect on their morphology*.

The ANOVA is reported in Table 4 with red cells indicating P values larger than .05. It shows that for inclined struts, the in-plane orientation affects the struts shape, roughness, and size. The effect of in-plane orientation on those morphological features is carefully analyzed.

4.2 | Effect of in-plane orientation

4.2.1 | Results

As explained earlier (Figure 2), inclined struts with different in-plane orientations β have been manufactured. Figure 6 represents the evolution of shape deviation, arithmetic roughness (R_a), maximum height of profile (R_t), and mechanical equivalent diameter as a function of the in-plane orientation.

The shape deviation as a function of the angle β is represented in Figure 6A. The struts present the largest shape deviation for an orientation of 5° and the smallest deviation for struts at -95° . The variation of maximum height of profile (R_t) in Figure 6C follows the same trend.

The mechanical equivalent diameter and arithmetic roughness as a function of β show two populations with low values for $\beta < 0^\circ$ and larger values for $\beta > 0^\circ$.

4.2.2 | Discussion

Two effects can influence part's quality as a function of its in-plane orientation. According to Figure 2, the recoater moves in the build plane along the x direction (from $x+$ to $x-$) and the argon flows in the y direction (from $y+$ to $y-$). They can both affect struts morphology.

Potential effects of the recoater

In order to give an explanation for the observed trends, the behavior of the strut during the recoating step in the manufacturing process has to be understood. At each layer, the recoater comes from $x+$ to $x-$ to spread powder onto the plate. The manufacturing of struts at 35.3° from the build plate without support is challenging. During manufacturing, the heat accumulation on the down-facing surface produces an overmelting of this zone (see Section 3.1), which induces a distortion of the part during manufacturing as presented in Figure 3. The part thus rises at each layer in the zone of the down-facing surface. When spreading the new layer of powder, the recoater carrying the powder can collide with the part and generate a change in the final shape. The amplitude of interaction relies on the following:

- The recoater path length, i.e., the maximum length of the strut in the x direction.
- The orientation of the strut during interaction—front ($\beta = \pm 135^\circ$) or back to the recoater directions ($\beta = \pm 45^\circ$).

Both effects can explain partially the variation in shape and roughness. Indeed, for a $\beta = 5^\circ$ orientation, the path length of the recoater onto the surface is maximum, whereas it is minimum for $\beta = \pm 95^\circ$. Moreover, struts facing the recoater direction ($\beta = \pm 135^\circ$) endure larger collision with the recoater than struts with an orientation $\beta = \pm 45^\circ$.

Potential effects of the argon flow

As seen in Figure 6B and D, large differences of roughness and mechanical equivalent diameters are visible between struts with a positive β orientation and a negative one. This variation cannot be explained by the recoater's action. The argon flow arises from $y+$ to $y-$ direction. For struts with a positive in-plane orientation, the argon flow reaches firstly the down-facing side of the strut, whereas for negative in-plane orientations, it arrives of the opposite side. It can affect the thermal environment on the down-facing surface and thus modify the distortion of the strut.

In situ monitoring of the process needs to be carried out to verify such hypothesis and to be able to discriminate the influence of the argon flow and the recoater.

5 | CONCLUSION

This study presents the systematic analysis of vertical and inclined struts as a function of their position and orientations using high-resolution X-ray tomography.

A methodology for the systematic analysis of the morphological features of struts is developed. It allows the extraction of strut shape (shape ratio and angle of equivalent ellipse), waviness, roughness (R_a and R_t), and size (inscribed, circumscribed, isovolume, and mechanical equivalent diameters).

The distinction between first-order and second-order parameters is carried out using this methodology and applying an ANOVA sensitivity approach.

The build orientation affects largely the morphology of the struts. Inclined struts have larger size, shape deviation, and waviness but lower porosity. On the contrary, the position of struts in the build plate does not influence their morphology. The in-plane orientation for inclined struts is a second-order parameter affecting strut shape, roughness, and size. The argon flow that modifies local thermal environment and the recoater that can interact with the struts during manufacturing could explain such variations.

ACKNOWLEDGEMENTS

This work has been carried out within the framework of the LASER project from the French Institute of Technology IRT Saint Exupery in collaboration with SIMaP laboratory. We are thankful to ANR and industrial partners for their funding of the project. The authors also gratefully acknowledge C. Josserond at SIMaP for his help with the tensile test monitoring.

CONFLICT OF INTEREST

The authors declare that they have no conflict of interest

ORCID

Mathieu Suard  <https://orcid.org/0000-0002-5504-3839>

REFERENCES

1. Schaedler TA, Jacobsen AJ, Torrents A, et al. Ultralight metallic microlattices. *Science*. 2011;334(6058)(80):962-965. <https://doi.org/10.1126/science.1211649>
2. Wadley HNG. Multifunctional periodic cellular metals. *Philos Trans A Math Phys Eng Sci*. 2006;364(1838):31-68. <https://doi.org/10.1098/rsta.2005.1697>
3. Evans AG, Hutchinson JW, Ashby MF. Multifunctionality of cellular metal systems. *Prog Mater Sci*. 1999;43(43):171-221.
4. Chougrani L, Pernot JP, Véron P, Abed S. Lattice structure lightweight triangulation for additive manufacturing. *CAD Comput Aided Des*. 2017;90:95-104. <https://doi.org/10.1016/j.cad.2017.05.016>
5. Deshpande VS, Fleck NA, Ashby MF. Effective properties of the octet-truss lattice material. *J Mech Phys Solids*. 2001;49:1747-1769.
6. Tancogne-Dejean T, Mohr D. Stiffness and specific energy absorption of additively-manufactured metallic BCC metamaterials composed of tapered beams. *Int J Mech Sci*. 2018;141(March):101-116. <https://doi.org/10.1016/j.ijmecsci.2018.03.027>
7. Lu TJ, Stone HA, Ashby MF. Heat transfer in open-cell metal foams. *Acta Mater*. 1998;46(10):3619-3635. [https://doi.org/10.1016/S1359-6454\(98\)00031-7](https://doi.org/10.1016/S1359-6454(98)00031-7)
8. Sundarram SS, Li W. The effect of pore size and porosity on thermal management performance of phase change material infiltrated microcellular metal foams. *Appl Therm Eng*. 2014;64(1-2):147-154. <https://doi.org/10.1016/j.applthermaleng.2013.11.072>
9. Heintz P, Müller L, Körner C, Singer RF, Müller FA. Cellular Ti-6Al-4V structures with interconnected macro porosity for bone implants fabricated by selective electron beam melting. *Acta Biomater*. 2008;4(5):1536-1544. <https://doi.org/10.1016/j.actbio.2008.03.013>

10. Murr LE, Gaytan SM, Medina F, et al. Next-generation biomedical implants using additive manufacturing of complex, cellular and functional mesh arrays. *Philos Trans A Math Phys Eng Sci.* 2010;368(1917):1999-2032. <https://doi.org/10.1098/rsta.2010.0010>
11. Leary M, Mazur M, Williams H, et al. Inconel 625 lattice structures manufactured by selective laser melting (SLM): mechanical properties, deformation and failure modes. *Mater Des.* 2018;157:179-199. <https://doi.org/10.1016/j.matdes.2018.06.010>
12. Gümrük R, Mines RAW, Karadeniz S. Static mechanical behaviours of stainless steel micro-lattice structures under different loading conditions. *Mater Sci Eng A.* 2013;586:392-406. <https://doi.org/10.1016/j.msea.2013.07.070>
13. Heinel P, Rottmair A, Körner C, Singer RF. Cellular titanium by selective electron beam melting. *Adv Eng Mater.* 2007;9(5):360-364. <https://doi.org/10.1002/adem.200700025>
14. Hernández-Nava E, Mahoney P, Smith CJ, Donoghue J, Todd I, Tammis-Williams S. Additive manufacturing titanium components with isotropic or graded properties by hybrid electron beam melting/hot isostatic pressing powder processing. *Sci Rep.* 2019;9(1):1-11. <https://doi.org/10.1038/s41598-019-40722-3>
15. Dallago M, Winiarski B, Zanini F, Carmignato S, Benedetti M. On the effect of geometrical imperfections and defects on the fatigue strength of cellular lattice structures additively manufactured via selective laser melting. *Int J Fatigue.* 2019;124(November 2018):348-360. <https://doi.org/10.1016/j.ijfatigue.2019.03.019>
16. Liu L, Kamm P, García-Moreno F, Banhart J, Pasini D. Elastic and failure response of imperfect three-dimensional metallic lattices: the role of geometric defects induced by selective laser melting. *J Mech Phys Solids.* 2017;107:160-184. <https://doi.org/10.1016/j.jmps.2017.07.003>
17. Sercombe TB, Xu X, Challis VJ, et al. Failure modes in high strength and stiffness to weight scaffolds produced by selective laser melting. *Mater Des.* 2015;67:501-508. <https://doi.org/10.1016/j.matdes.2014.10.063>
18. Delroisse P, Jacques PJ, Maire E, Rigo O, Simar A. Effect of strut orientation on the microstructure heterogeneities in AlSi10Mg lattices processed by selective laser melting. *Scr Mater.* 2017:32-35. <https://doi.org/10.1016/j.scriptamat.2017.07.020>
19. Suard M, Martin G, Lhuissier P, et al. Mechanical equivalent diameter of single struts for the stiffness prediction of lattice structures produced by electron beam melting. *Addit Manuf.* 2015;8:124-131. <https://doi.org/10.1016/j.tca.2013.09.026>
20. Zhang XZ, Tang HP, Leary M, Song T, Jia L, Qian M. Toward manufacturing quality Ti-6Al-4V lattice struts by selective electron beam melting (SEBM) for lattice design. *Jom.* 2018;70(9):1870-1876. <https://doi.org/10.1007/s11837-018-3030-x>
21. Lozanovski B, Leary M, Tran P, et al. Computational modelling of strut defects in SLM manufactured lattice structures. *Mater Des.* 2019;171:107671. <https://doi.org/10.1016/j.matdes.2019.107671>
22. Pérez-Sánchez A, Yáñez A, Cuadrado A, Martel O, Nuño N. Fatigue behaviour and equivalent diameter of single Ti-6Al-4V struts fabricated by electron beam melting orientated to porous lattice structures. *Mater Des.* 2018;155:106-115. <https://doi.org/10.1016/j.matdes.2018.05.066>
23. Amani Y, Dancette S, Delroisse P, Simar A, Maire E. Compression behavior of lattice structures produced by selective laser melting: X-ray tomography based experimental and finite element approaches. *Acta Mater.* 2018;159:395-407. <https://doi.org/10.1016/J.ACTAMAT.2018.08.030>
24. Dallago M, Zanini F, Carmignato S, Pasini D, Benedetti M. Effect of the geometrical defectiveness on the mechanical properties of SLM biomedical Ti6Al4V lattices. *Procedia Struct Integr.* 2018;13:161-167. <https://doi.org/10.1016/j.prostr.2018.12.027>
25. Persenot T, Burr A, Martin G, Buffière J-Y, Dendievel R, Maire E. Effect of build orientation on the fatigue properties of as-built electron beam melted Ti-6Al-4V alloy. *Int J Fatigue J.* 2019;118(11):65-76. <https://doi.org/10.1016/j.ijfatigue.2018.08.006>
26. Cunningham R, Narra SP, Montgomery C, Beuth J, Rollett AD. Synchrotron-based X-ray microtomography characterization of the effect of processing variables on porosity formation in laser power-bed additive manufacturing of Ti-6Al-4V. *Jom.* 2017;69(3):479-484. <https://doi.org/10.1007/s11837-016-2234-1>
27. Leicht A, Klement U, Hryha E. Effect of build geometry on the microstructural development of 316L parts produced by additive manufacturing. *Mater Charact.* 2018;143:137-143. <https://doi.org/10.1016/j.matchar.2018.04.040>
28. Ning Y, Wong YS, Fuh JYH, Loh HT. An approach to minimize build errors in direct metal laser sintering. *IEEE Trans Autom Sci Eng.* 2006;3(1):73-80. <https://doi.org/10.1109/TASE.2005.857656>
29. Bagheri ZS, Melancon D, Liu L, Johnston RB, Pasini D. Compensation strategy to reduce geometry and mechanics mismatches in porous biomaterials built with selective laser melting. *J Mech Behav Biomed Mater.* 2017;70:17-27. <https://doi.org/10.1016/j.jmbbm.2016.04.041>
30. Schneider CA, Rasband WS, Eliceiri KW. NIH Image to ImageJ: 25 years of image analysis. *Nat Methods.* 2012;9(28 June 2012):671-675.

How to cite this article: Suard M, Barrière L, Lhuissier P, Perusin S, Filloux B, Dendievel R. Influence of manufacturing orientations on the morphology of alloy 718 single struts manufactured by selective laser melting. *Mat Design Process Comm.* 2021;3:e140. <https://doi.org/10.1002/mdp2.140>